Large scale, multi-fidelity, multi-physics, hybrid RANS-LES of an installed aeroengine

J. C. Tyacke[a], M. Mahak[b] and P. G. Tucker[c]
Department of Engineering, University of Cambridge, Cambridge, CB3 0DY, UK

The aerodynamics and also noise produced by aeroengines is a critical topic in engine design. Hybrid Reynolds-Averaged Navier-Stokes-Large-Eddy Simulation (RANS-LES), is used to investigate the influence of upstream internal geometry on jet flow and noise. The methods are validated using an isolated nozzle. Internal geometry is added using approximated Immersed Boundary Methods (IBMs) and Body Force Methods (BFMs) reducing grid complexity and cost. Installed coaxial nozzles including an intake, wing and flap and internally, the fan, outlet guide vanes (OGVs) and other large features are modelled. These large scale multi-fidelity, multi-physics calculations are shown to reveal substantial new aeroacoustic insights into an installed aeroengine. The turbulence generated internally introduces a complex unsteady nozzle exit flow. This accelerates inner shear layer development moving it one jet diameter upstream and reduces the potential core length by 5%. For the more intense outer shear layer, the effect appears secondary.

[a] Senior Research Associate, Department of Engineering, University of Cambridge, Cambridge, CB3 0DY, UK, AIAA member.
[b] PhD Student, Department of Engineering, University of Cambridge, Cambridge, CB3 0DY, UK.
[c] Professor, Department of Engineering, University of Cambridge, Cambridge, CB3 0DY, UK, Associate fellow AIAA

Nomenclature

A = Flux Jacobian

Cv = Constant volume specific heat (J/kgK)

D = Nozzle bypass exit diameter (m)

F = Inviscid cell face flux

F_n = Force normal to blades (N)

F_p = Force parallel to blades (N)

K_n = Normal force coefficient

K_p = Parallel force coefficient

P_0 = Total pressure (Pa)

P_∞ = Total pressure (Pa)

T_0 = Total temperature (K)

T_∞ = Total temperature (K)

U_0 = Bypass exit velocity (≈ 300 m/s)

c_b = Blade chord (m)

c_d = Drag coefficient

i, j = Cells adjacent to cell face

d = True wall distance (m)

d_{int} = RANS-NLES Interface location (m)

$\tilde{d}$ = Modified wall distance (m)

h_b = Blade thickness (m)

$\dot{m}$ = Mass flow rate (Kg/s)

u, v = Axial, radial velocity (m/s)

x, y, z = Cartesian coordinates (m)

α = Blade metal angle

ε = Smoothing parameter

θ = Acoustics arc angle, azimuthal angle

∇^2 = Pseudo-Laplacian

ϕ = Flow variable

ρ = Density (kg/m^3)

o, i = outer, inner

I. Introduction

The aerodynamics of and noise produced by aeroengines is a critical topic in engine design. The increase in air travel and tightening emissions targets require both airframe and aeroengine designers to accurately predict performance and pollutant and noise emissions. As well as reducing green house gas emissions, the Advisory Council for Aeronautical Research in Europe (ACARE) has set the target of a reduction in perceived noise emission of 50% (to those of the year 2000) by the year 2020. To enable such challenging targets to be met, the importance of the many influences must be understood. These include the use of single or dual stream jet nozzles, the presence (or lack of) of a pylon, wing, flap and deflection angles, nozzle serrations, eccentricity, temperature and velocity ratio, flight stream and upstream/internal geometry effects. The latter effects are the main focus of this paper.

For dual stream jets, Viswanathan et al. [1] assess area ratio, velocity ratios and flight stream effects. Clear effects could be observed when controlling one parameter in isolation, however, in a design setting, any combination of parameters could be used. Using experiments and the SST $k-\omega$ RANS model, Mihaescu et al. [2] study a nozzle with and without pylon and wing effects. The flight stream elongates and radially confines the jet. The inclusion of a wing and pylon increases jet spreading and reduces turbulence production under the wing-pylon-nozzle.

The Ffowcs-Williams Hawkings (FWH) approach has been used with much success in conjunction with LES for the prediction of jet noise [3]. The use of a permeable FWH surface surrounding all noise sources avoids the expensive computation of volume source terms throughout the domain. For axi-symmetric domains, Mendez et al. and Wang et al. [3, 4] make use of multiple FWH surfaces to ensure the best surface placement (near the jet but far enough away from hydrodynamic effects). Nelson et al. [5] also provide some guidance on grid generation and FWH surface placement for an axi-symmetric single stream jets. For complex geometries the optimum FWH surface placement is not clear *a priori*. Paliath and Premasuthan [6] use a simplified surface that encompasses the entire geometry at a nearly uniform distance. Another method is to base the FWH surface on an iso-surface of mean turbulence kinetic energy [7].

The trend towards higher bypass ratio engines and closer integration with the airframe con-

stantly changes the design space. This makes the use of simple correlations less attractive if they are unable to capture the numerous effects mentioned adequately. In fact, Viswanathan et al. [1] suggest there is a dire need to update existing methods. Experimental facilities are expensive and it can be difficult to obtain certain data, for example, to include flight stream effects. The multiple interactions for complex geometry jets make RANS unsuitable due to separation, mixing and strong streamline curvature, among others. Real aerospace simulations have strong component couplings. This can be, for example, between, the engine and airframes. It can also be internal to the engine itself or between the fan and upstream and downstream zones. Modelling all this can give rise to a highly geometrically complex, large, multi-scale system. Set in this backdrop, eddy resolving methods such as LES and hybrid RANS-LES seem attractive.

Approximating such complex geometry can hence provide substantial computational savings. It has the additional benefit of simplifying mesh generation and can allow various geometries to be interchanged numerically, with little effort. The Immersed Boundary Method of Peskin [8] and related approaches to model the presence of walls such as direct and feedback forcing (see Fadlun [9] for an overview) have been used widely for simple geometries such as cylinders and wavy wall flows [10, 11]. Mochel et al. [12] use a first order IBM to represent chevrons on a jet nozzle, indicating agreement with experiments for first and second order flow statistics. Nelson et al. [5] use an IBM with local grid refinement to model nozzle serrations/chevrons. This avoids excessive grid resolution requirements. An immersed boundary condition technique coupled to a wall model was utilized by Seror et al. [13] for LES of full-scale detailed landing gear noise. Brunet [14] add turbulent inflow fluctuations to a Zonal Detached Eddy Simulation (ZDES) of an isolated and installed jet nozzle showing improved agreement with measurements and improved shock location prediction. Dudek [15] approximate the effect of vortex generators in a duct by adding a lift force source term, aligning the flow to the guide vanes.

Hale et al. Hsiao et al. [16] model an inlet with an axisymmetric representation of a fan and guide vanes to study angle of attack effects on intake flow separation showing consistency with experiments. Hale et al. [17] consider the coupling between a three-stage compressor with inlet distortion using such an approach. Eastwood [18] extend this beyond axi-symmetric smeared

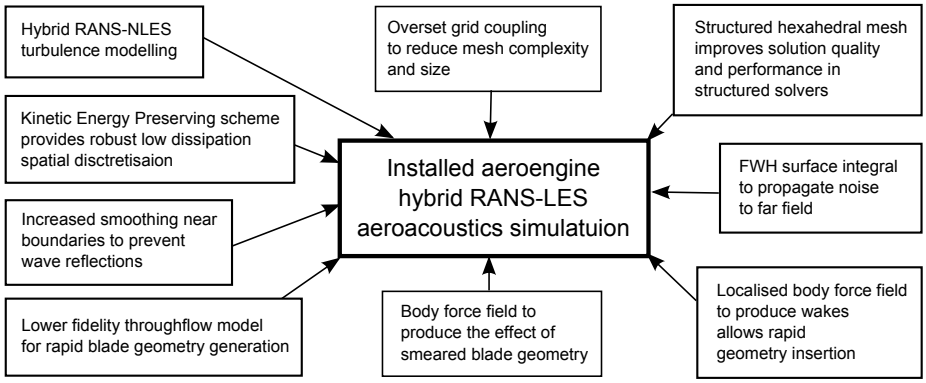

Fig. 1 Elements included in the current simulations for complex geometry jet aeroacoustics.

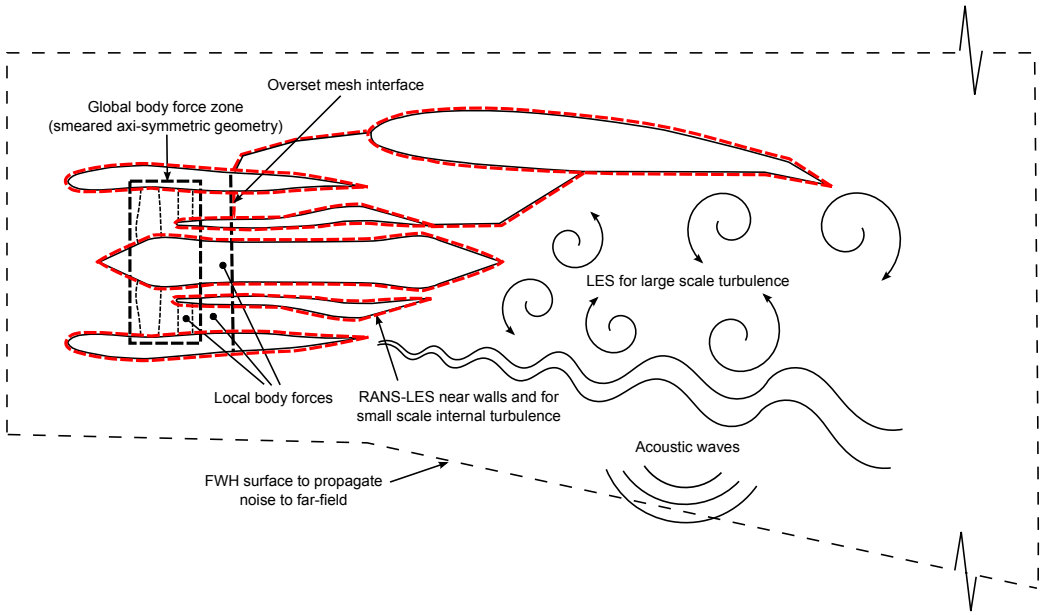

Fig. 2 Methods used to model the coupled multi-scale, multi-physics system. Note, the RANS-LES region employs RANS adjacent to walls only, reverting to LES elsewhere.

geometry to add blade geometry to the core flow stream of a coaxial jet nozzle. Similarly, here, we model the fan and vanes downstream of it using a body force field. Hence, the fan geometry is smeared. Additionally, when included, the wakes of other components downstream of the fan are discretely represented by localised body forces. These wakes include the downstream vanes, engine supporting frames (A-frames) and the gearbox shaft. A unified body force-IBM approach is outlined by Cao et al. [19].

Hybrid RANS-LES provides a method to increase understanding of aerodynamics and also acoustics. Where no explicit subgrid scale model is used, dissipation arising from suitable numer-

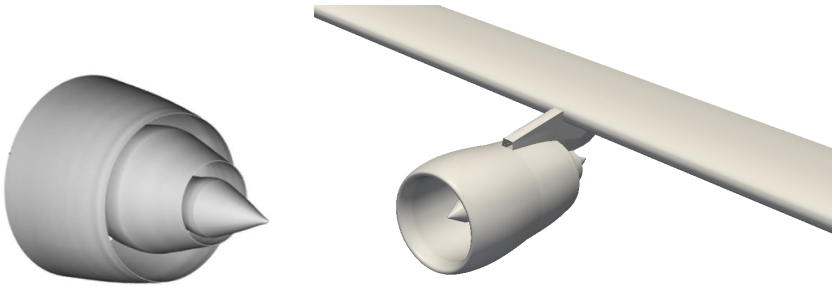

(a) COJEN nozzle (b) Fan-to-flap

Fig. 3 External geometries to be meshed.

ical schemes can be used in LES zones to produce Numerical-LES (NLES). This is attractive for industrial solvers that are often dissipative. Figure 1 indicates elements that are currently used to tackle the multi-scale and multi-physics challenges, arising in the modelling of complex geometry aeroengine jet flows. Figure 2 shows key modelling methods used for different zones of the studied geometry. This includes a near wall RANS layer as indicated by the red dashed line. We leverage various fidelity numerical methods to model a range of flow physics. These include, body force modelling of internal engine geometry, overset meshes, hybrid RANS-LES to model and resolve turbulence and propagation of the generated acoustic waves to the far field.

The paper is structured in the following way. The case setups are described. Then, numerical methods including the solver, BFM, turbulence modelling and acoustic processing are discussed. The results are then presented. The latter includes aspects of validation through comparison with clean jet data.

II. Case setup

Table 1 Jet nozzle boundary conditions.

	Bypass (Imposed directly for isolated nozzle)	Core (imposed directly for all cases)
P_0/P_∞	1.69	1.62
T_0/T_∞	1.16	3.09
$\dot{m}$ (Kgs^{-1})	9.325	1.633

An isolated nozzle shown in Fig. 3(a) is used for validation and two installed nozzle cases with BFM are modelled and compared. One without internal geometry feature wakes and one with

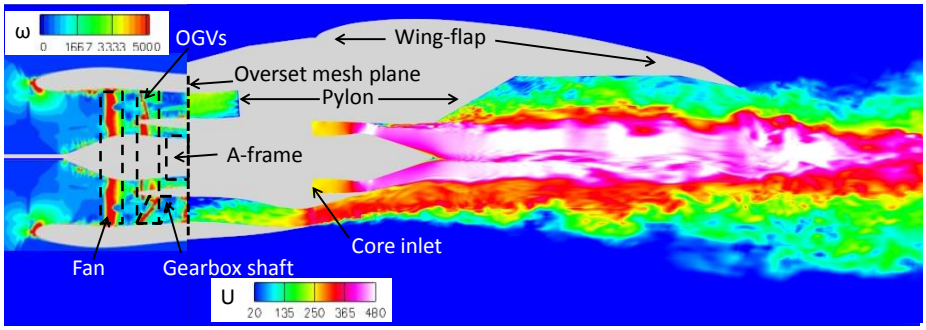

Fig. 4 Case setup showing geometric zones, with instantaneous internal vorticity magnitude (left of overset mesh plane) and axial velocity contours.

outlet guide vanes (OGV), A-frame and gearbox shaft wakes. Figure 3(b) shows the installed engine geometry to be meshed. The original geometry including the COJEN coaxial jet nozzle, pylon, wing and flap geometry as Xia et al. [20] is modified by adding simple axi-symmetric intake, hub and splitter geometry upstream. Converging radial grid lines upstream of the spinner created small cells restricting time step size. Hence this central core was considered as an inviscid wall, having negligible impact on the overall flow. The two geometries are interfaced using overset meshes at a plane in the bypass duct only. Using the BFM, the boundary conditions are matched closely to that of the original COJEN nozzle at the overset mesh plane by running a precursor RANS simulation. The target boundary conditions are provided in Tab. 1 where $P_\infty = 101,325$ Pa and $T_\infty = 288.15$ K. Overall, the boundary conditions are matched to within 2-5% using the BFM at the bypass duct overset mesh plane. The core stream is not interfaced with the upstream zone, hence boundary conditions are exactly applied directly at the nozzle core inlet.

The different geometrical zones are indicated in Fig. 4. Vorticity can be seen throughout the bypass duct and near geometrical features (for example, near the gear box shaft). The considerable internal geometry creates a complex bypass duct flow. To contrast the flow produced with included upstream internal geometry, a baseline case is also run, which uses the axi-symmetric BFM in the fan and OGV zones only. This maintains comparable conditions between the two installed nozzle cases allowing a contrast between the jet flow with and without internally generated turbulence in the bypass duct.

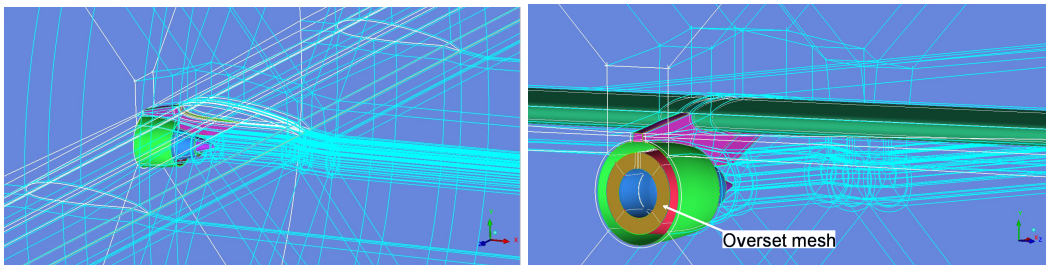

(a) Side view of the rear mesh blocking. (b) Upstream view showing the bypass duct.

Fig. 5 Rear grid structured blocking.

A. Mesh

The presence of a pylon wing and flap introduce great mesh blocking complexity. These features intersect many O-grids creating a highly complex grid topology as shown in Fig. 5. It was for this reason an overset mesh interface (shown in Fig. 5(b)) was chosen so that grids were not complicated further. The rear jet mesh is similar to that used by Xia et al. [20], but with more circumferential nodes in order to resolve wakes in the bypass duct. The upstream mesh is axi-symmetric with approximately 90 nodes per OGV blade passage (approx. 5-10 per h_b). The first off wall grid node is located at $y^+ \approx 1$. The total mesh size is 100 million cells. The use of the BFM is highly cost effective for modelling gross flow features. For the isolated nozzle validation case, a mesh of 7 million nodes is used. A 50 million cell mesh is used for acoustics.

III. Numerical Methods

A. Governing Equations

The governing equations for (U)RANS/LES are based on the conservative form of the Navier-Stokes equations as per the continuity and momentum equations (1–4) below.

$$\frac{\partial \rho}{\partial t} + \frac{\partial \rho \tilde{u}_j}{\partial x_j} = 0 \tag{1}$$

$$\frac{\partial \rho \tilde{u}_i}{\partial t} + \frac{\partial \rho \tilde{u}_i \tilde{u}_j}{\partial x_j} = -\frac{\partial \tilde{p}}{\partial x_i} + \frac{\partial \tilde{\tau}_{ij}}{\partial x_j} \tag{2}$$

The symbol $\tilde{u}_i$, ρ, μ, $\tilde{p}$, t and x, represent velocity components, density, viscosity (from Sutherland's equation), static pressure, time and spatial coordinate respectively. The stress tensor $\tilde{\tau}_{ij}$ is

calculated using

$$\tilde{\tau}_{ij} = 2(\mu + \mu_T)\left[\tilde{S}_{ij} - \frac{1}{3}\frac{\partial \tilde{u}_j}{\partial x_j}\delta_{ij}\right] \tag{3}$$

where δ_{ij} is the Kronecker delta ($\delta_{ij} = 1$ if $i = j$ or zero otherwise). The strain rate tensor $\tilde{S}_{ij} = \frac{1}{2}\left(\frac{\partial \tilde{u}_i}{\partial x_j} + \frac{\partial \tilde{u}_j}{\partial x_i}\right)$. The tilde and T subscript are used to indicate that traditional RANS is used near walls and NLES elsewhere. In the RANS region $\mu_T = \mu_t$ and in the NLES region $\mu_T = \mu_{SGS} = 0$.

The corresponding total energy equation is expressed as

$$\frac{\partial \tilde{E}}{\partial t} + \frac{\partial(\tilde{u}_j(\tilde{E} + \tilde{p}))}{\partial x_j} = \frac{\partial(\tilde{u}_i \tilde{\tau}_{ij})}{\partial x_j} - \frac{\partial \tilde{q}_j}{\partial x_j} \tag{4}$$

Here, the total energy per unit volume $\tilde{E} = \rho e + \frac{1}{2}\rho \tilde{u}_i \tilde{u}_i$, where $e = C_v T$ and pressure, temperature (T) and density are related through the equation of state for a perfect gas $\tilde{p} = \rho R \tilde{T}$. For the heat flux $\tilde{q} = -(k + k_T)\frac{\partial \tilde{T}}{\partial x_j}$, where k is the thermal conductivity and $k_T = C_p \mu_T / Pr_T$. $Pr_T = 0.9$ in RANS regions. In NLES zones, $\mu_T = 0$ hence $k_T = 0$

B. Turbulence modelling

To alleviate near wall grid requirements a hybrid RANS-NLES model is used. This has been used with success for jets and other complex flows [18, 21]. Near walls the Spalart-Allmaras RANS model [22] is used to model the inner boundary layer below $y^+ = 60$. Outside of the RANS layer where larger scales dominate, NLES is used to resolve complex unsteady flow features. The wall distance in the NLES zone is brought to zero causing $\mu_T = 0$. To provide a smooth transition from the RANS to NLES, the true wall distance is modified using a Hamilton-Jacobi equation. This is shown in Eq. (5).

$$|\nabla \tilde{d}| = 1 + f(\tilde{d})\nabla^2 \tilde{d} + g(d) \tag{5}$$

The RANS wall distance is replaced with the modified wall distance. Near walls the eikonal equation (producing the exact wall distance) solution is obtained from the first two terms. Near

the RANS-NLES interface, $g(d) = \varepsilon_1(d/d_{int})^n$ biases the transition, whilst the Laplacian term multiplied by $f(\tilde{d}) = \varepsilon_0\tilde{d}$ provides a smooth function. The three parameters $n = 4$, $\varepsilon_0 = 1.2$ and $\varepsilon_1 = 7.5$ [18]. This retains accurate wall distances nearest the wall, then smoothly returns the wall distance to zero for the NLES region. Further smoothing is hence not required. Figure 6 displays the modified wall distance and the resulting RANS and NLES regions.

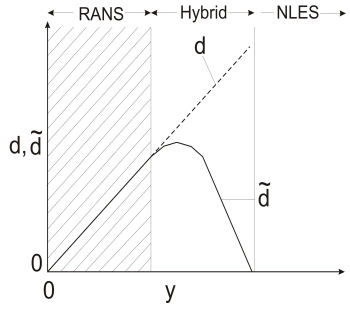

Fig. 6 Wall distance/blending function from the Hamilton-Jacobi equation.

C. Discretisation

An unstructured finite volume, edge-based, compressible solver is used. For temporal integration, an implicit second order backward difference scheme is used with dual time-stepping, with inner iterations solved using an explicit 5-stage Runge-Kutta scheme [23]. A second order kinetic energy preserving (KEP) discretisation [24] is used in space with numerical smoothing adapted for jet simulations. The KEP inviscid cell face flux with additional numerical smoothing is given below by equation (6).

$$F_{ij} = \frac{1}{2}(\rho_i + \rho_j) \times \frac{1}{2}(u_i + u_j) \times \frac{1}{2}(\phi_i + \phi_j) - \frac{1}{2}\varepsilon|A|[\nabla_i^2\phi - \nabla_j^2\phi] \tag{6}$$

The KEP scheme is based on the skew symmetric operator [24] and provides a stable numerical method that is non-dissipative and conserves kinetic energy. The first right hand side terms in (6) relate to the KEP scheme with the last providing numerical smoothing. This fourth order smoothing provides the minimal dissipation required for eddy resolving methods, also reducing dispersion errors and maintaining general solution stability. The smoothing is minimised in the turbulent and acoustic regions and increased near farfield boundaries to prevent wave reflections. The parameter ε is used

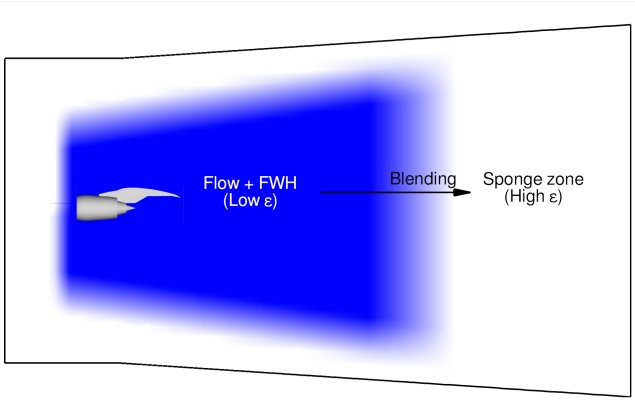

Fig. 7 Numerical smoothing applied in the computational domain (not to scale).

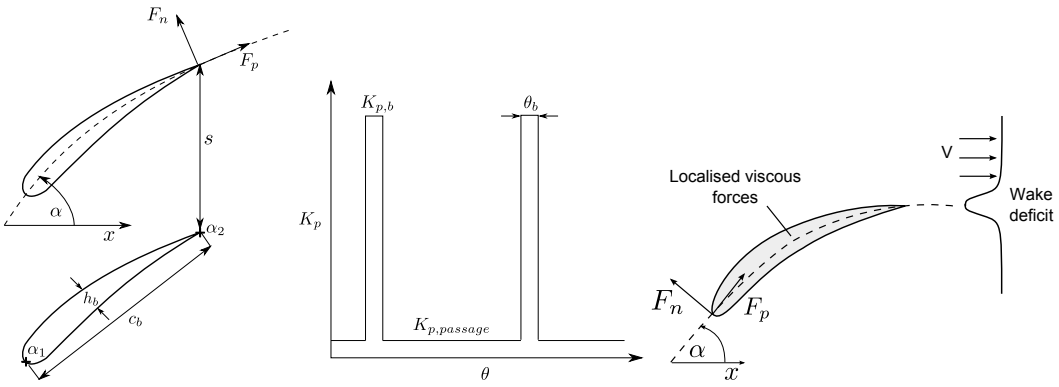

(a) Body force nomencalture.

(b) Wake function example.

(c) Wake modification.

Fig. 8 BFM diagrams showing (a), the overall method and nomenclature, (b), the wake function used and (c), the wake function effect in relation to an OGV.

to control numerical dissipation in the central jet flow and acoustic region as shown in Fig. 7.

D. Body force modelling

Although the BFM can be considered as a throughflow model, it is not a classic two-dimensional actuator duct model but consists of a three-dimensional locally axisymmetric Navier-Stokes solver with body forces [25]. The implemented model has been validated previously [18, 26]. The aerodynamic effects of a blade row are modelled using the assumption of an infinite number of blades with an axisymmetric flow in each infinitesimal blade passage and body forces are added as source terms of the Navier-Stokes equations on the right hand side of the momentum and energy equations. This is formulated primarily to give tangency of flow to the notional blades using trigonometric identities.

In ducts and gap regions between blade rows the source terms or body forces will be inactive. The body forces are divided into components parallel and normal to the local blade metal angle. This is illustrated in Fig. 8(a). The forces normal and parallel (F_n and F_p respectively) are also illustrated. These forces, which could be considered as lift and drag forces, are uniformly distributed in the volume defined by the blade row chord, c_b and span, s. The forces are mapped to cylindrical coordinates as $F_{n,x}, F_{n,\theta}$ and $F_{p,x}, F_{p,\theta}, F_{p,r}$ respectively and have the form of equations (7)-(8) for inertial and viscous related force terms, where the function f contains trigonometric terms.

$$F_{n,x} = \frac{K_n}{s}\frac{V_\theta}{V_{rel}} f(V_x, V_\theta, \alpha), F_{n,\theta} = -\frac{K_n}{s}\frac{V_x}{V_{rel}} f(V_x, V_\theta, \alpha) \tag{7}$$

$$F_{p,x} = \frac{K_p}{s} V_x V_{rel}, \;\; F_{p,\theta} = -\frac{K_p}{s} V_\theta V_{rel}, \;\; F_{p,r} = -\frac{K_p}{s} V_r V_{rel} \tag{8}$$

Here, Vx, V_θ, V_r are the velocity components respectively in the axial, tangential and radial direction and V_{rel} the local relative fluid velocity. α represents the local blade metal angle and s is the blade pitch as indicated in Figure 8(a). Hence, these forces can be used to approximate a rotor or stator blade row. However, due to the axi-symmetric assumption, no wakes are produced, only the time-mean flow turning and subsequent pressure rise through the rotor and flow straightening through the guide vanes.

1. Fan and guide vane modelling

The fan is modelled using the axi-symmetric BFM. For the case without internal features, the axi-symmetric BFM is again used for the OGVs. Each zone is defined by the axial extent of the blade region. This results in smeared geometry, with flow turning and pressure rise obtained through the fan and flow straightening through the OGVs. The blade metal angles required are obtained from a through-flow model to provide the target operating conditions. This BFM is used for both installed nozzles.

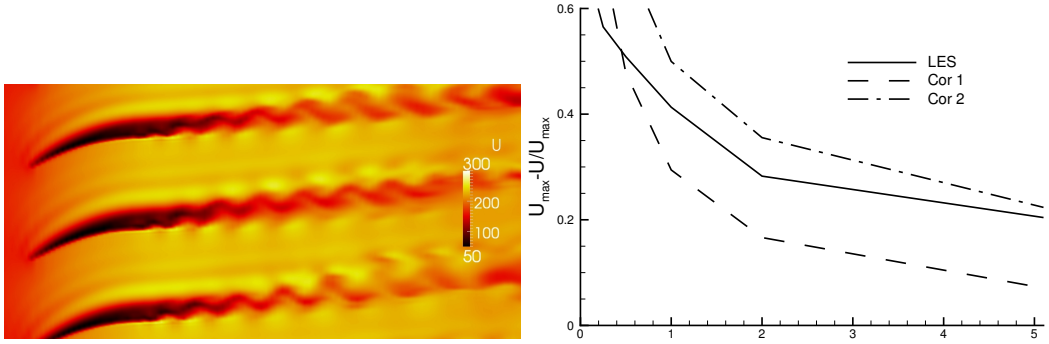

(a) Axial velocity contours near the OGVs.

(b) Velocity decay.

Fig. 9 OGV wakes and velocity decay.

2. Wake modelling

For the installed nozzle with internal geometry features, 19 outlet guide vanes (similar to [27]) are modelled using the above model with localised wakes. The original model is thus modified in order to produce blade wakes. In the region occupied by the OGV blades, the viscous effects are modelled by increasing the constant K_p (increasing the body force parallel to the blade surface). This is shown in Fig. 8(c). To retain the overall viscous loss, K_p is reduced in the blade passage. A square wave is is thus defined to set the value of K_p based on circumferential position θ. This is shown in Fig. 8(b).

$$\frac{u_{max} - u}{u_{max}} = \frac{2.42\sqrt{c_d}}{0.6 + \frac{2d}{c_b cos\alpha}} \tag{9}$$

$$\frac{u_{max} - u}{u_{max}} = \frac{1.6\sqrt{c_d}}{(\frac{\chi}{c_b cos\alpha} + 0.025)^{1/2}} \tag{10}$$

Figure 9(a) shows axial velocity contours near the OGVs. The wakes are calibrated to provide realistic velocity decay. As shown in Fig. 9(b), the wake using LES lies between two correlations (labelled Cor.1 and Cor.2 [28], assuming a drag coefficient of 0.1). The correlations are given by equations (9) and (10) respectively, where $d = x_{te}/c_b$ is the distance from the OGV trailing edge, c_b, the blade chord and the metal angle, $\alpha = 0$. The form of (10) was found to be most similar to other authors [29], the $\sqrt{c_d}$ term stemming from Prandtl mixing theory. In [30], (9) showed the best

fit to measurements. Other internal geometry is also modelled in a similar manner. The A-frames and gearbox shaft are also large features that generate wakes in the bypass flow. Again, the BFM is modified. By setting $\alpha = 0$ and increasing K_p within the zone occupied by geometry, body forces can be used to generate wakes.

E. Acoustic processing

The original form of the FWH equation [31] involves a volume integral term, which is expensive to calculate. However, it is negligibly small when all noise sources lie within an enclosed, permeable FWH surface and is hence ignored. The acoustic signal is captured as a time series on a permeable FWH surface and the resulting far-field pressure fluctuations p' are later calculated from surface integrals using an FWH solver. In the absence of the volume integral, the FW-H surface should encompass all the sound sources in the jet. At the surface, spurious noise can be generated by hydrodynamic disturbances of the flow rather than the acoustic signal. The use of multiple FWH surfaces has proven to be useful in ensuring only acoustic signals are being recorded at the surface and not vortical/hydrodynamic signals. The ideal placement of FWH surfaces is challenging *a priori*, hence the use of mutiple surfaces allows more data to be recorded. Agreement of overall sound pressure levels (OASPLs) between different surfaces in regions of adequate grid resolution indicates a form of FWH surface placement convergence. This has been shown for single stream jets [4]. When a closing disc is placed at the downstream end of the FWH surface, it can also suffer from the passing vortical structures and generate spurious hydrodynamic noise [3, 4, 32]. This is a particular issue for jets with an external flight stream (not studied here), where vortices will be strongly convected through the FWH surface and far downstream. However, with a closing disc, at low angles relative to the axial flow, there is potential for acoustic predictions to become more accurate as more of true sound source can be captured. The question of whether to close the FWH surface at the outlet or whether to use downstream closing discs is hence, an open question.

Here, data is recorded for both scenarios. The multiple FWH surfaces are indicated in Fig. 10(a), where contours show mean axial velocity. For the current validation case, Fig. 10(b) indicates a single FWH surface with multiple closing discs. The temporal pressure gradient clearly show the instantaneous hydrodynamic and acoustic pressure field. The overall sound pressure level (OASPL)

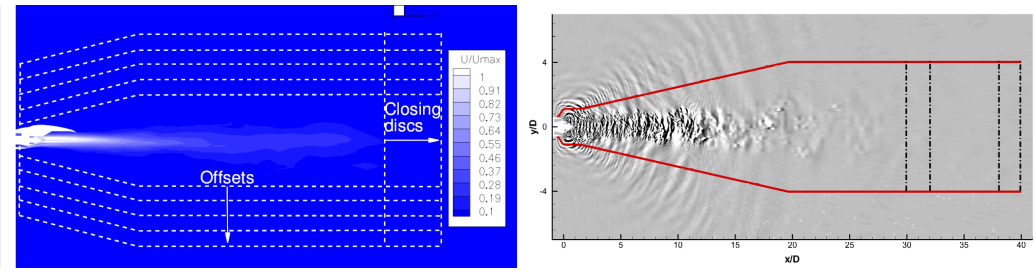

(a) Multiple surface schematic.

(b) Isolated nozzle FWH surface placement.

Fig. 10 FWH surface placement with: (a) u contours, (b) dp/dt contours.

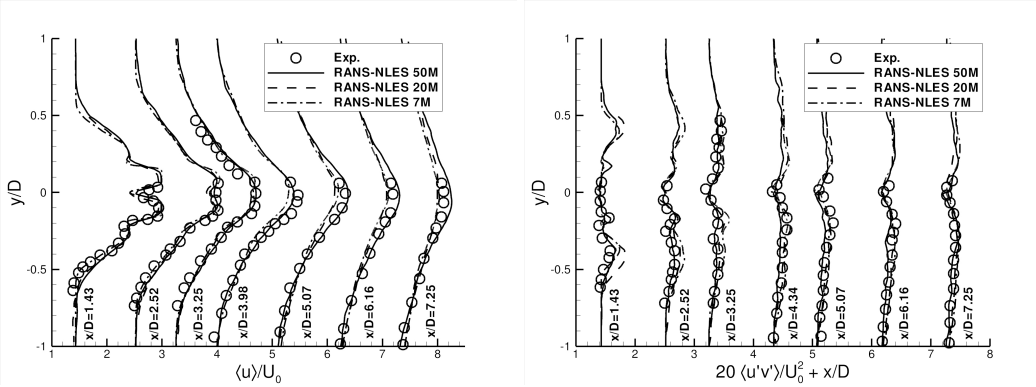

(a)

(b)

Fig. 11 Flow validation of the isolated nozzle. The solid lines, dashed lines and symbols represent the present 7 and 50 million (7M and 50M), Eastwood 20 million (20M) [21] calculation and measurements respectively.

is projected from the FWH surface to the far field at $100D$. The angles for the OASPL are measured from the positive x- axis. The flow is developed and time-averaged, each for $100t^*$, where $t^* = D/U_0$, requiring approximately 350,000 and 1,500,000 core hours for the 50 million cell isolated and 100 million cell installed cases respectively. Note, an unstructured flow solver was used, carrying overhead, hence we expect additional mesh improvements and more efficient solvers to reduce this cost significantly.

IV. Results

A. Isolated nozzle

Figure 11(a) and 11(b) show validation of time averaged velocity and shear stress, showing an encouraging match with measurements for the 7 million cell grid. Similar agreement is found

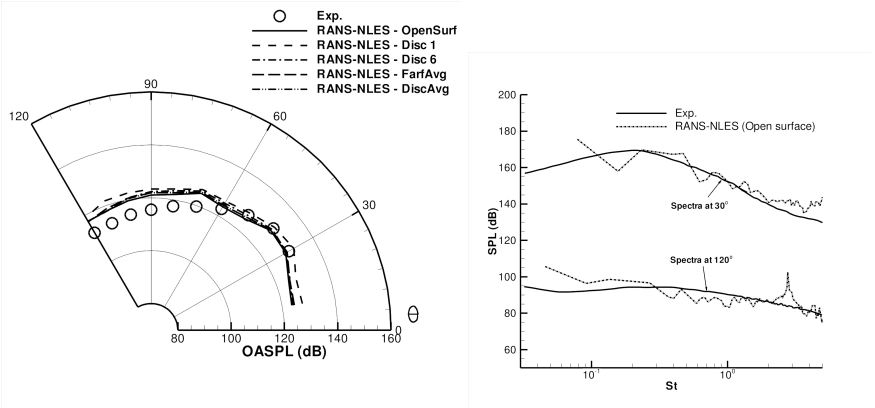

(a) OASPL. (b) Spectra.

Fig. 12 Acoustic validation of the isolated nozzle

with the 50 million cell mesh used for acoustics and with simulations performed by Eastwood [21] (using a 20 million cell mesh). There is some degree of asymmetry in the measured data (due to, for example nozzle eccentricity issues) [33], however, the hybrid RANS-NLES correctly models the true, axi-symmetric flow.

Figures 12(a) and 12(b) show the azimuthally averaged OASPL predictions and spectra comparison of the isolated nozzle simulation with measured noise levels. Noise is measured with an array of microphones. The azimuthal centre is taken along the jet centreline (x-axis). Figure 12(a) shows OASPL prediction using different parts of the FWH surface. When using an open surface and partially closed disc at the downstream end, OASPL levels are 1-2 dB lower than measured values. This is also observed when using farfield averaging and disc averaging (described in detail in [4]). This can be attributed to the FWH surface loosing some of the emitted sound pressure waves for the open surface and partially closed disc and over cancelling of noise while using averaging techniques. All the predictions are able to capture correct OASPL at the peak noise propagation direction i.e. 30°. After $\theta = 60°$, a rise in OASPL prediction is observed for all cases. This can be explained using spectra for 120° in Fig. 12(b). We see high frequency tonal noise in the spectra which is not physical. This may well be due to laminar type structures near the lip caused by lack of grid resolution and a boundary layer that does not contain resolved turbulence structures. These factors would promote transition helping to remove this artefact.

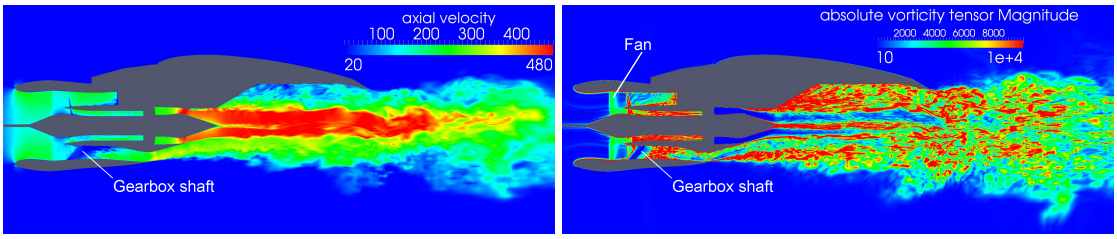

(a) Axial velocity contours (z-plane). (b) Vorticity magnitude contours (z-plane).

Fig. 13 Velocity and vorticity contours.

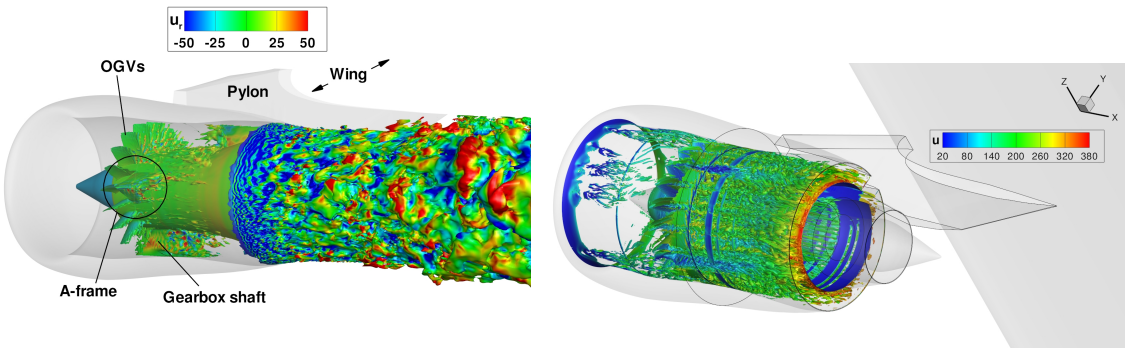

(a) (b)

Fig. 14 (a) Velocity magnitude iso-surfaces showing internal geometry and developing jet plume coloured by radial velocity and (b), Q-criterion iso-surface showing duct turbulence coloured by axial velocity.

B. Fan-to-flap

Figure 13(a) shows instantaneous axial velocity contours in the z-plane. The gear box shaft is visible in the lower half of the bypass duct. Figure 13(b) also makes more visible the fan zone at the left. The internal geometry of this case can be seen in Fig. 14(a). Note, this does not clearly show the turbulence inside the duct. The velocity magnitude iso-surfaces indicate wake producing geometry and the developing jet plume coloured by radial velocity. The duct turbulence is shown more clearly in Fig. 14(b). The internal flow and jet plume can be seen in Figs. 15(a) and 15(b), producing larger structures near the wing, smaller internal scales generated from the BFM and middle sized eddies generated on the underside of the jet plume. Hence, the flow is clearly multi-scale, requiring a range of numerical fidelity methods.

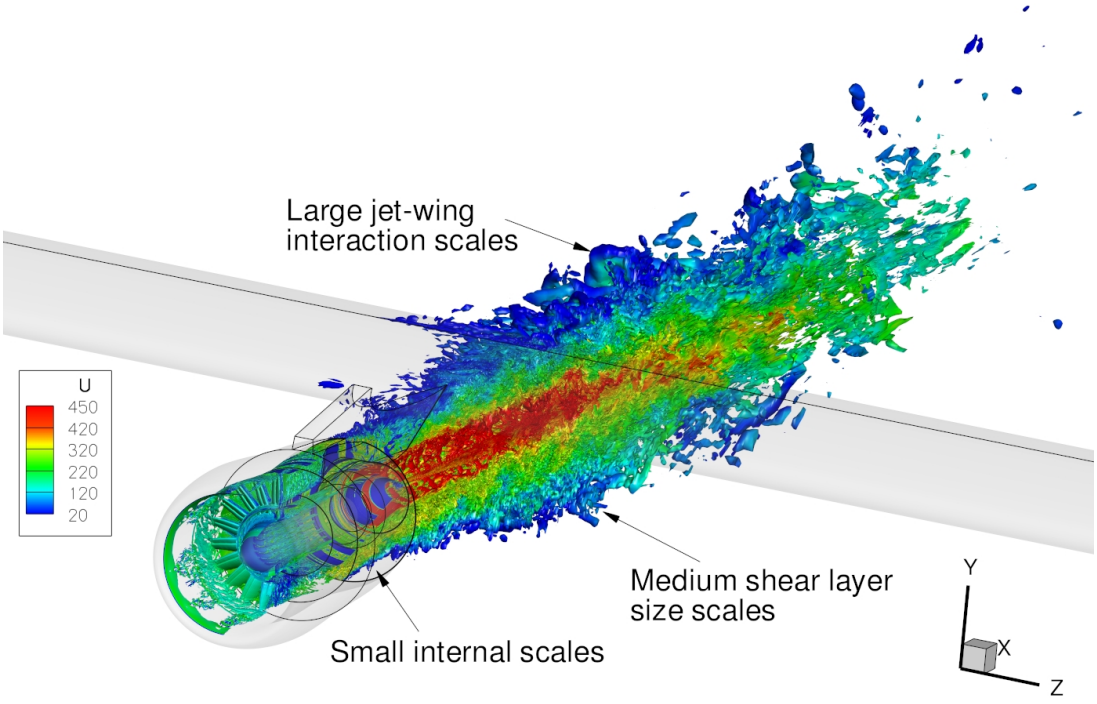

(a)

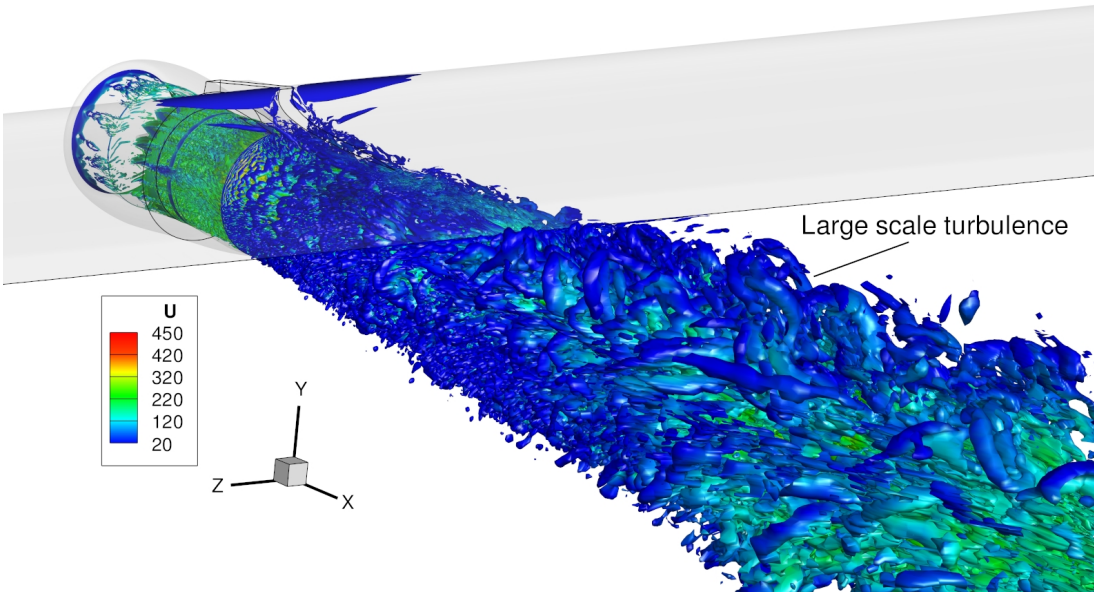

(b)

Fig. 15 Q-criterion of the internal and external flow.

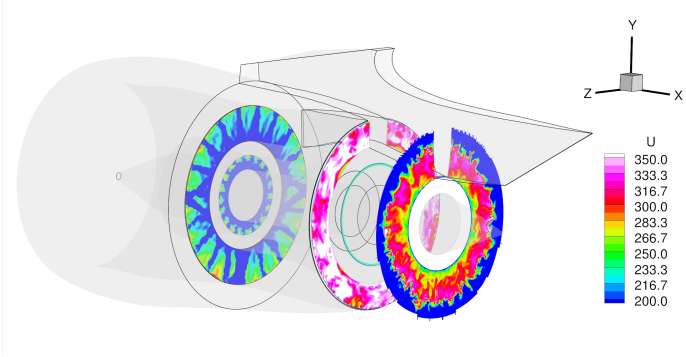

Fig. 16 Axial planes showing instantaneous axial velocity contours in the bypass duct.

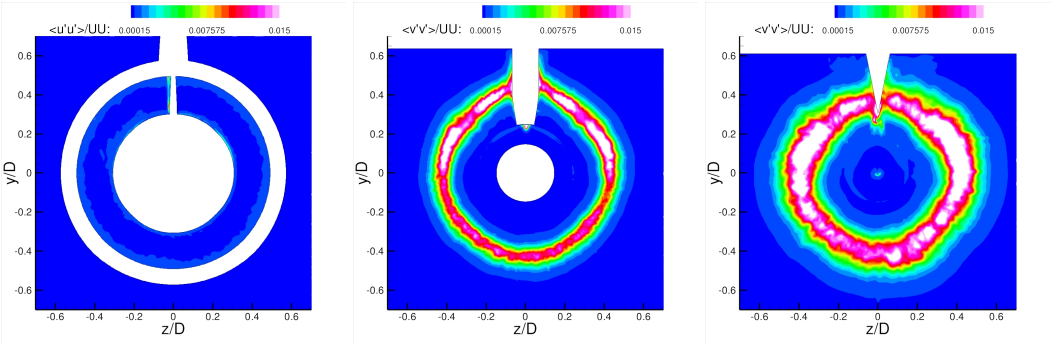

(a) $x/D = -0.5$ No wakes (b) $x/D = 0.5$ No wakes (c) $x/D = 1.0$ No wakes

(d) $x/D = -0.5$ With wakes (e) $x/D = 0.5$ With wakes (f) $x/D = 1.0$ With wakes

Fig. 17 Axial and radial Reynolds stress contours.

1. Axial plane contours

Figure 16 shows axial velocity contours at different axial planes. From left to right, these are just downstream of the internal geometry, at the bypass exit plane and halfway along the pylon. The wakes from the internal geometry can be seen to the left of the figure and produce a complex unsteady exhaust stream.

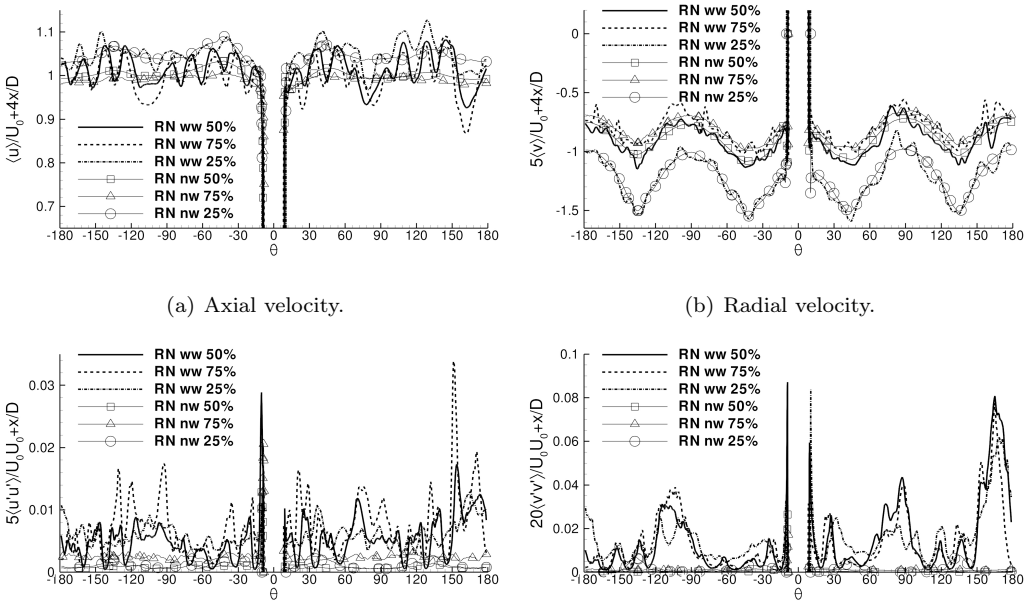

(a) Axial velocity.

(b) Radial velocity.

(c) Axial Reynolds stress.

(d) Radial Reynolds stress.

Fig. 18 Azimuthal profiles at 50%, 75% and 25% bypass duct radius.

Figure 17 displays axial and radial Reynolds stress contours for different axial planes near the bypass duct exit ($x/D = -0.5, 0.5, 1.0$). Figure 17(a) shows the axial Reynolds stress contours inside the bypass duct with no wakes and is hence nearly uniform. Figures 17(b) and 17(c) show radial contours at $0.5D$ and $1D$ downstream of the bypass exit respectively. The contours are nearly circular (concentric), with regions of higher turbulence generated near the pylon and wing (white regions at the top of the figures). Figure 17(d) indicates the wakes from the OGVs, A-frames (AF) and gearbox shaft (GB) which are slightly rotated around the duct by residual swirl. Figure 17(e) - 17(f) shows the effect of the AF and GB remains downstream, increasing the turbulence levels in the secondary shear layer in the lower y/D portion.

2. Azimuthal variation of mean velocity and Reynolds stresses

Figure 18 shows the azimuthal variation of mean axial and radial velocity and Reynolds stresses at the bypass duct exit. The thicker lines represent the flow with wakes and the symbol-lines the flow without wakes. The solid, dashed and dot-dashed lines represent profiles at a radius of 50%, 75% and 25% of the bypass (BP) duct radius ($R_{BP,o} - R_{BP,i}/(R_{BP,o} - R_{BP,i})$) respectively. The

mean axial velocity with no wakes (nw) in Fig. 18(a) shows a wavy profile due to the presence of the pylon ($\theta = 0$). The duct flow with wakes (ww) clearly shows the presence of the A-frames at $\theta \approx \pm 90°$. The GB wake can be seen at $\theta \approx 160°$. In addition to these elements, the OGVs appear superimposed over the nw profiles. In Fig. 18(b), the negative radial velocity towards the jet centreline at the exit again can be seen to be nonuniform. There is a shorter wavelength variation imposed with wake features compared to the profiles with no wakes. In Fig. 18(c), the wakes produce around 5% turbulence intensity. The axial Reynolds stresses are highest at the outer radius (dashed line). Figure 18(d) plots radial stresses, more clearly showing the presence of the A-frames and gearbox shaft. Without wakes the radial fluctuation is negligible. The intensity is lower than that of the axial component (3% based on U_0), however, this component will tend to penetrate the primary and secondary shear layers increasing mixing. Again, the outer and center radius profiles show higher peaks.

3. Axial variation of mean velocity and Reynolds stresses

Shown in Fig. 19 are axial velocity profiles taken downstream of the nozzle exit. In Fig. 19(a),the peak velocity near the centreline for the jet with wakes shifts downward relative to the jet without wakes. Increased mixing from the bypass turbulence more rapidly smooths out the mean velocity profile. This can be seen in Fig. 19(b) at $z/D \approx \pm 0.2$

Due to the large magnitude of the primary and secondary shear layer turbulence, the upstream turbulence effect does not appear pronounced. However, figures 20(a) and 20(b) show an earlier and greater peak in the inner shear layer at $y/D \approx -0.2$ for x/D =1,1.5 and 2. This effect, mainly from the GB, also produces more radial mixing as indicated at $y/D \approx -0.4, x/D = 0$ to $y/D \approx -0.15, x/D = 2$. The effect can be more clearly seen in Fig 21 which contrasts Reynolds shear stress contours with (Fig. 21(a)) and without (Fig. 21(b)) wakes. A threshold value of 0.05 is chosen to define the shear layer edges. Indicated by the vertical line in each, the bypass turbulence causes an intensification of the initial inner shear layer, causing it to migrate upstream by approximately $1D$. The edges of the shear layers are also indicated showing the two shear layers merging further upstream. The weaker inner shear layer is more heavily influenced by turbulent perturbations than

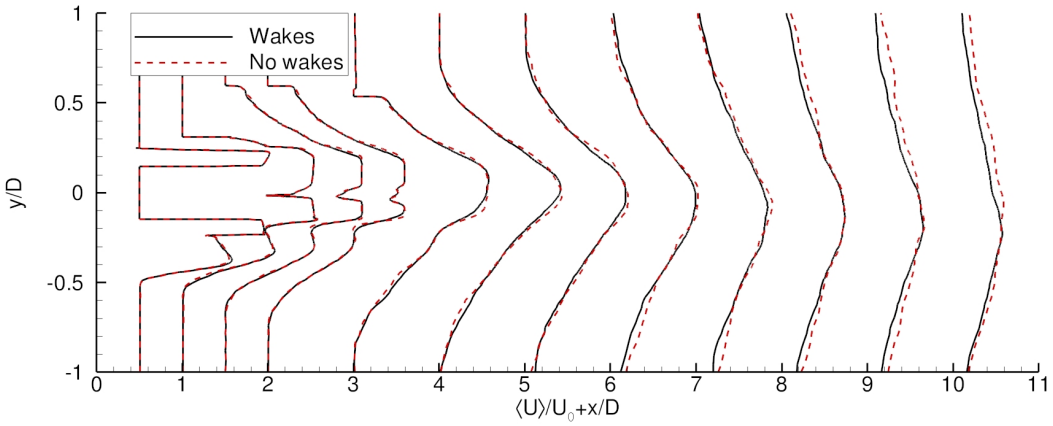

(a) $z = 0$ plane

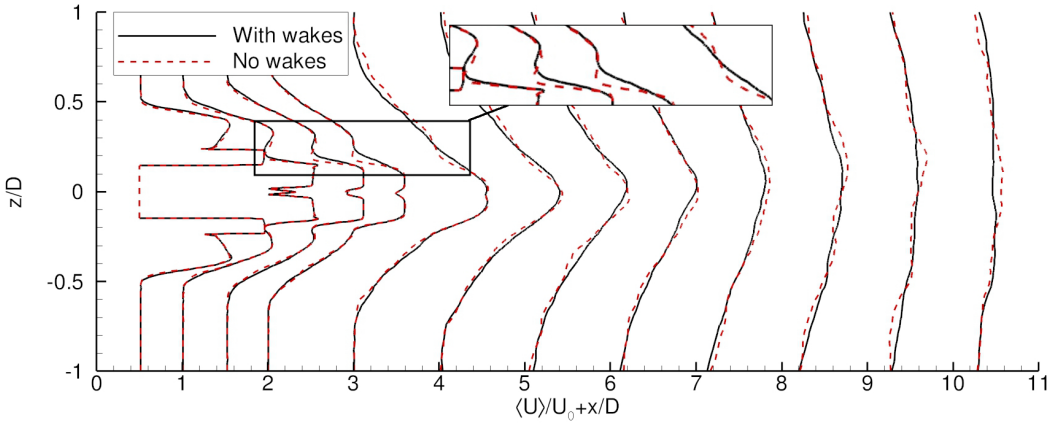

(b) $y = 0$ plane

Fig. 19 Downstream axial velocity profiles in: (a) $z = 0$ plane, (b) $y = 0$ plane.

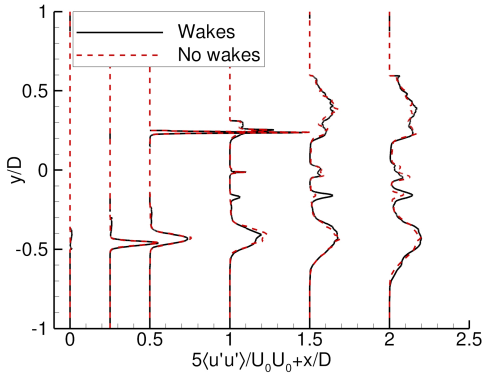

(a) $z = 0$ plane

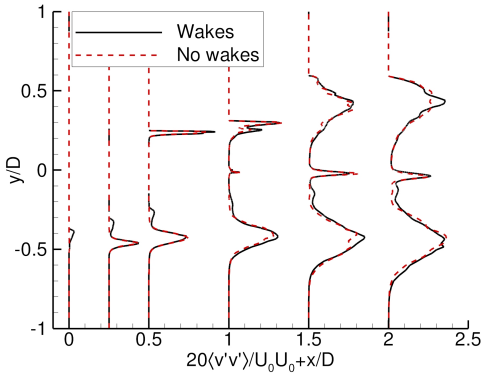

(b) $z = 0$ plane

Fig. 20 Axial and radial Reynolds stress profiles in the $z = 0$ plane.

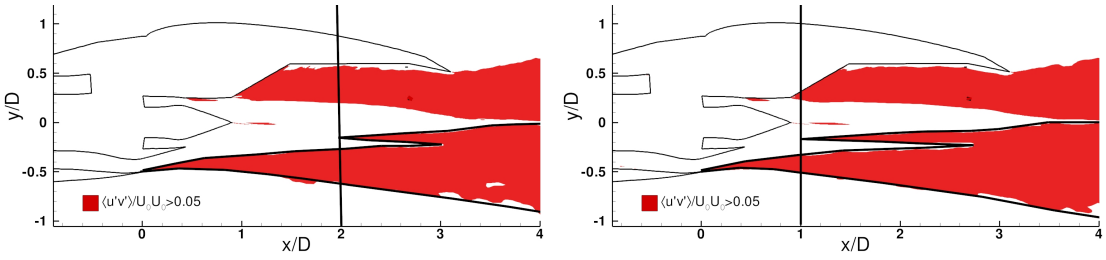

(a) $z = 0$ plane (b) $z = 0$ plane

Fig. 21 Shear stress contours ($\langle u'v' \rangle / U_0 U_0$): (a) No wake, (b) with wake.

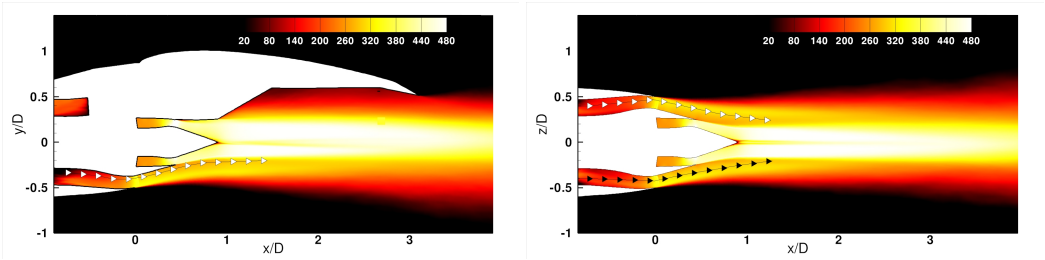

(a) $z = 0$ plane (b) $y = 0$ plane

Fig. 22 Profiles extracted along streamlines with mean axial velocity contours.

the stronger outer shear layer. Note that there is no flight stream in this case. Hence with a flight stream, the outer shear layer will naturally become weaker and the impact of adjacent disturbances will be more pronounced. The overall effect will however be dependent on the relative magnitude of the turbulence and velocity ratio between each fluid stream.

4. Streamline and axial profiles

Profiles extracted as shown in Fig. 22(a) are plotted in Fig. 23(a) and 23(b) for axial and radial Reynolds stresses respectively. For both quantities, after an initial decay before the nozzle exit, the remaining turbulence is substantially higher than the bypass duct without any turbulence. Similarly for the profile with white symbols in Fig. 22(b), the A-frames produce similar behaviour, as shown in Figs. 23(c) and 23(d). In the bypass duct, the flow is accelerated and hence pushed towards laminar flow (with no wakes the flow is already laminar). Laminarised flows, especially on curved surfaces can give rise to overshoots in Reynolds stresses at recovery. The external shear layer perhaps amplifies this, resulting in peaks near the bypass exit. We note this behaviour is well

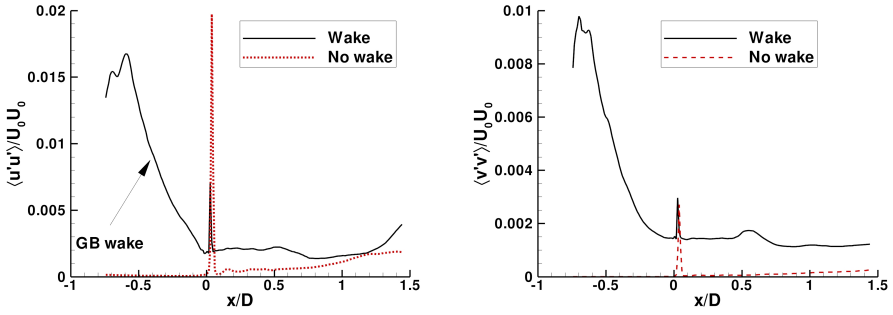

(a) $z = 0$ plane (b) $z = 0$ plane

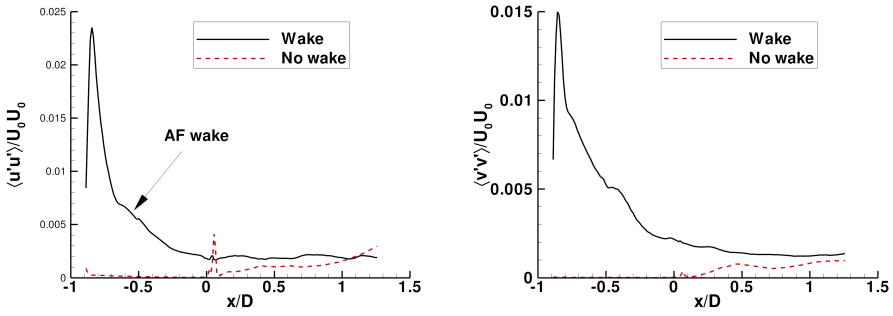

(c) $y = 0$ plane (d) $y = 0$ plane

Fig. 23 Axial and radial Reynolds stress profiles extracted along streamlines of Fig. 22, (a-b) in the $z = 0$ plane, (c-d) in the $y = 0$ plane. Note, U_0 is the bypass exit velocity.

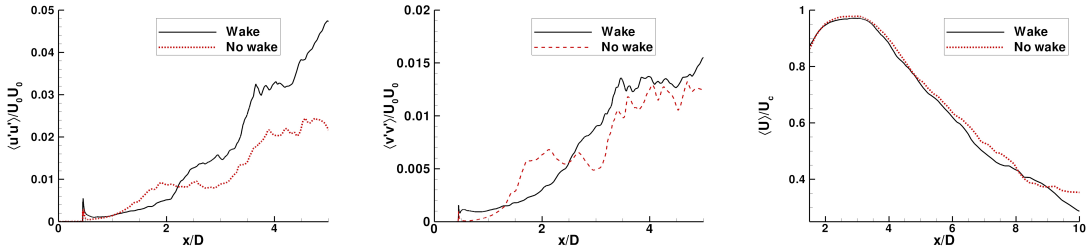

(a) (b) (c)

Fig. 24 Profiles extracted axially at: (a,b) the primary shear layer nozzle lip at $y/D = 0, z/D = 0.25$ and (c) the centreline.

resolved on the grid.

Taking an axial profile at the inner nozzle lip at $y/D = 0, z/D = 0.25$, Figs. 24(a) and 24(b) show an overall increase in turbulence levels of up to 100% when upstream turbulence is introduced. Downstream, the additional mixing reduces the potential core length as shown in Fig. 24(c) by approximately 5%. The alteration of the potential core length and shear layer development is likely

to change the noise signature produced. The noise level, directivity and spectral shape may all be changed, however this needs to be confirmed.

V. Conclusion

Body force modelling has been used to model the presence of blade rows, blade wakes and other large scale geometrical features in the bypass duct of an installed aeroengine. The use of BFM is shown to be a cost effective way of rapidly introducing geometry using existing or simplified grids. The introduction of upstream turbulence generated by large scale features initiated earlier shear layer development and thickening and greater azimuthal non-uniformity. The effect of such internal geometry may have an impact on overall noise levels, directivity and spectra. Using such methods, the design space can be widened and more rapidly explored using BFM as no re-meshing is required. Hybrid RANS-(N)LES can also be used to explore true flight conditions, generating data for complex configurations which can then improve more simple models for design use.

Acknowledgments

This work made use of the facilities of HECToR, the UK's national high-performance computing service, which is provided by UoE HPCx Ltd at the University of Edinburgh, Cray Inc and NAG Ltd, and funded by the Office of Science and Technology through EPSRC's High End Computing Programme. We also acknowledge PRACE for awarding us access to resource HERMIT based in Germany at HLRS Stuttgart. We also acknowledge funding under the EPSRC grant EP/I010440/1.

References

[1] Viswanathan, K., Czech, M. J., and Lee, I. C., "Towards Prediction of Dual-Stream Jet Noise: Database Generation," in "49th AIAA Aerospace Sciences Meeting including the New Horizons Forum and Aerospace Exposition," AIAA, Orlando, Florida, January, 2011.

[2] Mihaescu, M., Semlitsch, B., Fuchs, L., and Gutmark, E. J., "Airframe installation effects on the jet exhausting a coaxial nozzle system of a gas turbine engine," in "ASME Turbo Expo 2012," , 2012, pp. 1–9.

[3] Mendez, S., Shoeybi, M., Lele, S. K., and Moin, P., "On the use of the Ffowcs Williams-Hawkings equation to predict far-field jet noise from large-eddy simulations," *International Journal of Aeroacoustics*, Vol. 12, No. 1+2, 2013, pp. 1–20.

[4] Wang, Z.-N., Tucker, P., and Strange, P., "Far Field Noise Prediction of Subsonic Hot and Cold Jets Using Large-Eddy Simulation," in "Proceedings of ASME Turbo Expo 2014," ASME, Dusseldorf, Germany, 2014.

[5] Nelson, C., Cain, A., Du, Y., Morris, P., and Spyropoulos, J., "GT2013-94703 Toward Efficient Computational Aeroacoustic Analysis of High Speed Jets," pp. 1–14.

[6] Paliath, U. and Premasuthan, S., "Large Eddy Simulation for Jet Installation Effects," *19th AIAA/CEAS Aeroacoustics Conference*, pp. 1–10,
doi:10.2514/6.2013-2137.

[7] Langtry, R. B., Larssen, J. V., Winkler, C. M., Dorgan, a. J., and Mani, M., "DDES and Acoustic Prediction of Rudimentary Landing Gear Experiment Using Unstructured Finite Volume Methods," *Flow, Turbulence and Combustion*, Vol. 91, No. 3, 2013, pp. 717–745,
doi:10.1007/s10494-013-9487-3.

[8] Peskin, C. S., "Numerical analysis of blood flow in the heart," *Journal of Computational Physics*, Vol. 25, No. 3, 1977, pp. 220–252,
doi:10.1016/0021-9991(77)90100-0.

[9] Fadlun, E., Verzicco, R., Orlandi, P., and Mohd-Yusof, J., "Combined Immersed-Boundary Finite-Difference Methods for Three-Dimensional Complex Flow Simulations," *Journal of Computational Physics*, Vol. 161, No. 1, 2000, pp. 35–60,
doi:10.1006/jcph.2000.6484.

[10] Tseng, Y., "A ghost-cell immersed boundary method for flow in complex geometry," *Journal of Computational Physics*, Vol. 192, 2003, pp. 593–623,
doi:10.1016/j.jcp.2003.07.024.

[11] Lima E Silva, A. L. F., Silveira-Neto, A., and Damasceno, J. J. R., "Numerical simulation of two-dimensional flows over a circular cylinder using the immersed boundary method," *Journal Of Computational Physics*, Vol. 189, No. 2, 2003, pp. 351–370,
doi:10.1016/S0021-9991(03)00214-6.

[12] Mochel, L., Weiss, P.-É., and Deck, S., "Zonal Immersed Boundary Conditions: Application to a High-Reynolds-Number Afterbody Flow," *AIAA Journal*, Vol. 52, No. 12, 2014, pp. 1–13,
doi:10.2514/1.J052970.

[13] Seror, C., Sagaut, P., and Belanger, A., "A numerical aeroacoustics analysis of a detailed landing gear," in "10th AIAA/CEAS Aeroacoustics Conference," AIAA, Manchester, UK, 2004.

[14] Brunet, V., "Random flow generation technique for civil aircraft jet simulations with the ZDES approach," in Fu S, Haase W, Peng S-H, S. D., ed., "Progress in Hybrid RANS-LES Modelling, Notes on Numerical Fluid Mechanics and Multidisciplinary Design," Springer, pp. 193–204, 2012, doi:1007/978-3-642-31818-4_17.

[15] Dudek, J. C., "Modeling Vortex Generators in a Navier-Stokes Code," *AiIAA Journal*, Vol. 49, No. 4, 2011, pp. 748–759, doi:10.2514/1.J050683.

[16] Hsiao, E., Naimi, M., Lewis, J. P., Dalbey, K., Gong, Y., and Tan, C., "Actuator Duct Model of Turbomachinery Components for Powered-Nacelle Navier-Stokes Calculations," *Journal of Propulsion and Power*, Vol. 17, No. 4, 2001, pp. 919–927, doi:10.2514/2.5825.

[17] Hale, A., Davis, M., and Sirbaugh, J., "A Numerical Simulation Capability for Analysis of Aircraft Inlet-Engine Compatibility," *Journal of Engineering for Gas Turbines and Power*, Vol. 128, No. 3, 2006, p. 473, doi:10.1115/1.1925649.

[18] Eastwood, S., *Hybrid LES-RANS of complex geometry jets*, Ph.D. thesis, University of Cambridge, 2010.

[19] Cao, T., Hield, P., and Tucker, P. G., "Hierarchical immersed boundary method with smeared geometry," in "54th AIAA Aerospace Sciences Meeting, AIAA Science and Technology Forum and Exposition," AIAA, 2016.

[20] Xia, H., Tucker, P. G., Eastwood, S., and Mahak, M., "The influence of geometry on jet plume development," *Progress in Aerospace Sciences*, Vol. 52, No. 0, 2012, pp. 56–66, doi:10.1016/j.paerosci.2011.12.003.

[21] Eastwood, S., Tucker, P., Xia, H., and Klostermeier, C., "Developing Large Eddy Simulation for Turbomachinery Applications," *Phil. Trans. R. Soc. A*, Vol. 367, No. 1899, 2009, pp. 2999–3013.

[22] Spalart, P. R. and Allmaras, S. R., "A one-equation turbulence model for aerodynamic flows," *La Recherche Aérospatiale*, Vol. 1, No. 1, 1994, pp. 5–21.

[23] Hirsch, C., *Numerical Computation of Internal and External Flows*, John Wiley and Sons, 1990.

[24] Jameson, A., "Formulation of Kinetic Energy Preserving Conservative Schemes for Gas Dynamics and Direct Numerical Simulation of One-Dimensional Viscous Compressible Flow in a Shock Tube Using

Entropy and Kinetic Energy Preserving Schemes," *Journal of Scientific Computing*, Vol. 34, No. 2, 2007, pp. 188–208,
doi:10.1007/s10915-007-9172-6.

[25] Gong, Y., *A Computational Model for Rotating Stall and Inlet Distortions in Multistage Compressors*, Phd thesis, Massachusetts Institute of Technology, 1998.

[26] Loiodice, S., Tucker, P. G., and Watson, J., "Modelling of Coupled Open Rotor Engine Intakes," in "48th AIAA Aerospace Sciences Meeting Including the New Horizons Forum and Aerospace Exposition," AIAA, Orlando, Florida, January, 2010, pp. 2010–840.

[27] Nallasamy, M. and Envia, E., "Computation of rotor wake turbulence noise," *Journal of Sound and Vibration*, Vol. 282, No. 3-5, 2005, pp. 649–678,
doi:10.1016/j.jsv.2004.03.062.

[28] de Sousa, J. F. L., *Passive noise control for rotor-OGV interaction noise*, Ph.D. thesis, Universidade Tecnica de Lisboa, 2011,
doi:10.1177/0956797612465819.

[29] Dittmar, J., "Methods for reducing blade passing frequency noise generated by rotor-wake-stator interaction," Tech. rep., NASA, 1972.

[30] Kemp, N. H., "The Unsteady Forces Due to Viscous Wakes in Turbomachines," *Journal of the Aeronautical Sciences*, Vol. 22, No. 7, 1955, pp. 478–483.

[31] Ffowcs Williams, J. E. and Hawkings, D. L., "Sound Generation by Turbulence and Surfaces in Arbitrary Motion," *Phil. Trans R. Soc. A*, Vol. 264, 1969, pp. 321–342,
doi:10.1098/rsta.1969.0031.

[32] Casalino, D. and Hazir, A., "Computation of dual-stream unsteady jet flows and noise," pp. 12–16.

[33] Birch, S. F., "A Review of Axisymmetric Jet Flow Data for Noise Applications," *12th AIAA/CEAS Aeroacoustics Conference (27th AIAA Aeroacoustics Conference)*.